Pergamon

Int. J. Heat Mass Transfer. Vol. 40, No. 7, pp. 1521–1533, 1997

0017-9310/97 $17.00+0.00

PII: S0017-9310(96)00227-X

Numerical simulation of two- and three-dimensional free convection flows in a horizontal porous annulus using a pressure and temperature formulation

M. C. CHARRIER-MOJTABI

Institut de Mécanique des Fluides de Toulouse, UMR CNRS/INP/UPS no. 5502, Avenue du Professeur Camille Soula, 31400 Toulouse, France

(*Received* 24 *December* 1994 *and in final form* 24 *June* 1996)

Abstract—A numerical investigation of two-dimensional and three-dimensional free convection flows in a saturated porous horizontal annulus heated from the inner surface is carried out, using a Fourier–Galerkin approximation for the periodic azimuthal and axial directions and a collocation-Chebyshev approximation in the confined radial direction. The numerical algorithm integrates the Darcy–Boussinesq's equations formulated in terms of pressure and temperature. This method gives an accurate description of the 2-D multicellular structures for a large range of Rayleigh number and radii ratio. Some considerations about the existence of the various 2-D solutions previously described in the literature are reported. The 3-D spiral flows are described in the vicinity of the transition from the 2-D unicellular flows. Bifurcation points between 2-D unicellular flows and either 2-D multicellular or 3-D flows are also determined numerically.

1. INTRODUCTION

Buoyancy-driven flow and heat transfer in a porous layer bounded by two horizontal isothermal concentric cylinders have been the subject of a number of investigations over the last twenty years. This is due to the relevance of such a geometry in many technological applications such as thermal storage systems, cryogenics, underground electrical transmission lines, nuclear reactors, etc.

Although a large number of papers have dealt with two-dimensional natural convection in a horizontal porous annulus, very few deal with the three-dimensional free convective flows. However, three dimensional convective flows occur within the porous annulus for low Rayleigh numbers as demonstrated by Caltagirone [1]. In that investigation, Caltagirone [1] showed that in a cell of large longitudinal aspect rato ($A = 20$) and radii ratio $R = 2$, 3-D perturbations appear at the top of the annulus even for low Rayleigh numbers. The presence of these 3-D perturbations increases the overall heat transfer compared to the one obtained for 2-D flows.

The 2-D unicellular flows have been studied by several numerical approaches such as the finite difference method (Caltagirone [1], Burns and Tien [2]), finite element method (Mojtabi *et al.* [3]) or Galerkin spectral method (Charrier-Mojtabi and Caltagirone [4], Rao *et al.* [5] and Himasekhar and Bau [6]). For these flows, some perturbation solutions have been also proposed (Caltagirone [1] and more recently Mojtabi *et al.* [7] using a symbolic algebra code).

The Galerkin spectral method has been also used by several investigators [5, 6, 8] to describe the 2-D multicellular flows which appear in the annulus for Rayleigh numbers larger than a critical Rayleigh number depending on the radii ratio of the two cylinders. Charrier-Mojtabi *et al.* [8], have shown that the Fourier–Chebyshev method gives a better accuracy than the full Fourier–Galerkin method for the description of these 2-D multicellular flows. Some authors have also studied effects of the eccentricity on the overall heat transfer like Himasekhar and Bau [9].

Experimental studies using the Christiansen effect to visualize the thermal 2-D fields have been carried out by Cloupeau *et al.* [10] for the description of 2-D flows with a cell of longitudinal aspect ratio of $A = 0.5$ and a radii ratio of $R = 2$. They only observed unicellular flows. Charrier-Mojtabi *et al.* [8], with a cell of dimensionless parameters $A = 0.5$ and $R = 2$, using the Christiansen effect, have also observed unicellular steady structures and have shown experimentally the physical existence of 2-D bicellular steady structures for Rayleigh numbers higher than $65(\pm 5)$, with one small counterrotating cell at the top of the annulus. For $Ra^* > 65$, either a 2-D unicellular flow or a 2-D bicellular flow can be observed for the same value of Ra^* and each one of them is stable. In an eccentric annulus, Bau *et al.* [11] have obtained numerically, for the same set of dimensionless parameters (for example, $R = 2$, eccentricity of 0.6, $Ra^* = 200$), either an unicellular steady flow or a multicellular convective structure with two small counterrotating cells at the top of the annulus. However, their observations made

NOMENCLATURE

$A = l/r_i$ longitudinal aspect ratio of the cell
g gravitational acceleration
$H = l/(r_o - r_i)$ longitudinal aspect ratio based on the thickness of the layer
K permeability of the porous matrix
M, N, L order of approximation
l axial length of the cell
Nu_g^* global Nusselt number
P dimensionless pressure
r coordinate in radius direction scaled by r_i
r_i, r_o inner and outer cylinder radii
R ratio of the outer to the inner radius
Ra^* Rayleigh number of filtration: $Ra^* = (g\beta(T_i - T_0)(\rho c)_f K r_i)/\lambda^* \nu$
T dimensionless temperature
T_i, T_o inner and outer cylinder temperatures
X transformed coordinate, $\ln(r)$
Y transformed coordinate, ϕ
Z axial dimensionless coordinate.

Greek symbols
α $1/\ln(R)$
β coefficient of thermal expansion for the fluid
ε porosity of the porous medium
λ^* effective thermal conductivity of the saturated porous medium
ν kinematic viscosity of the fluid
ρ density of the fluid
$(\rho c)f$ heat capacity of the fluid
ϕ angular coordinate.

Subscripts
c critical
i inner
o outer.

in a Hele–Shaw cell demonstrate the existence of only unicellular structures. They attempted to artificially induce multicellular flows, but the multicell structure observed turned out to be unstable and after a period of time the unicellular flow regime was reconstructed. So, this multicellular flow, which is a mathematical solution of the problem, does not seem to have a physical existence. Since higher heat transport rates are associated with the multicellular flows, it seems important to establish which type of flow is physically realizable.

Stability analysis have been performed in refs. [1, 6]. In ref. [1], the transition between 2-D unicellular flows and 3-D flows with two-dimensional axisymmetrical perturbations depending on r and z (the radial and axial coordinates respectively) were investigated. Based on physical considerations, this stability analysis has been limited to the upper part of the annular layer and the axisymmetric 2-D disturbances considered were $\theta = \theta(r)\exp(isz)$ for the temperature and $u = u(r)\exp(isz)$; $w = w(r)\exp(isz)$ for the velocity components in the radial and axial directions respectively (s denotes the wavenumber). In ref. [6], the authors have considered the transitions between the 2-D multicellular flows using 2-D perturbation analysis.

In addition to experimental measurements of temperature by means of thermocouples, Caltagirone [1] has developed a 3-D finite element code, but no significant results have been obtained to confirm the description of the three-dimensional flow patterns. Using a finite difference model, Fukuda *et al.* [12] analyzed the case of inclined annuli, but their results could not be extended to the case of a horizontal annulus. Charrier-Mojtabi *et al.* [13] used the Fourier–Galerkin spectral method to expand the temperature and the velocity, but only low orders of approximation were considered. In fact the main numerical results concerning the 3-D flows are due to Rao *et al.* [14]. These authors used the Galerkin method and developed the temperature and the potential vector into truncated Fourier series. They described the steady 3-D flows with orders of approximation up to $10 \times 13 \times 5$ in r-, ϕ- and z-directions respectively. Due to the symmetry of the boundary conditions, they assumed that the 3-D flows are symmetrical with respect to the vertical plane containing the cylinders' axis and also with respect to the medium plane normal to the axis. In their study, only one value of the radii ratio, $R = 2$, was considered for a longitudinal aspect ratio, $H = 2$, and Rayleigh numbers varying between 60 and 150.

In the same configuration, but for a fluid medium, some investigations have been made by Cheddadi *et al.* [5] for 2-D flows, by Rao *et al.* [16] and Vafai *et al.* [17] for 3-D flows. The numerical technique used for all these works was a finite difference method.

In the present work, the 2-D and 3-D equations are solved to study in detail the possible free convection regimes in a horizontal porous annulus. Thus, an accurate numerical method, based on a mixed Fourier–Chebyshev approximation, is used with a new formulation in terms of pressure and temperature. For the 3-D case, this new formulation needs only two variables instead of four required for the classical formulation previously encountered in the literature. Up to 45 collocation points and 135 Fourier modes are used for the developments of the pressure and the temperature solutions to obtain an accurate description of the 2-D multicellular flows and to analyse

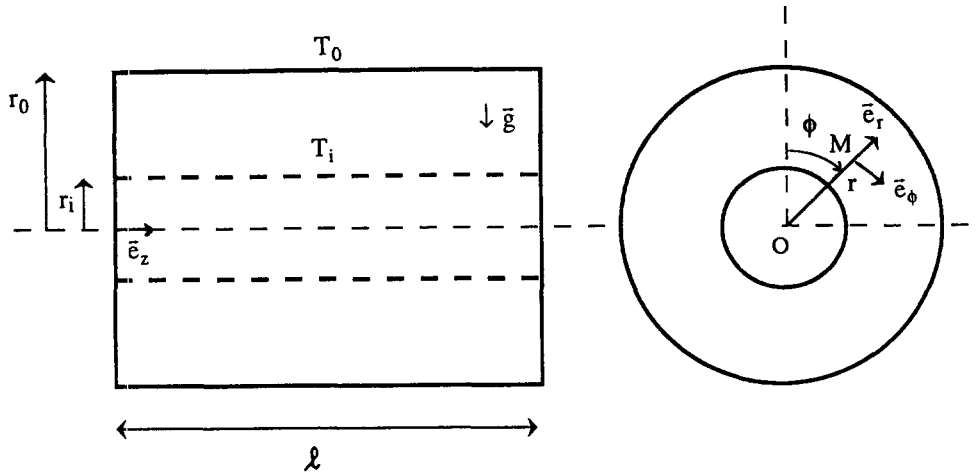

Fig. 1. Physical configuration and coordinates system.

the existence of the multiple 2-D solutions. Thus, the criteria of transition between the 2-D unicellular flow and these 2-D multicellular flows are determined numerically, for $R = 2$ and $R = 2^{1/2}$. For the 3-D case, we are mainly interested in the characterization of the 3-D flows in the vicinity of the transition from the 2-D unicellular flows. Near the transition point, the 3-D flow is quite regular, so only orders of approximation up to $16 \times 16 \times 16$ have been considered. However, the orders of approximation investigated in the present work are higher than those previously used by Rao *et al.* [14]. Several values of non-dimensional parameters (R, H) have been investigated ($R = 2$, $H = 2$; $R = 2$, $H = 1$; $R = 2^{1/2}, H = 2$) and the critical Rayleigh number of the transition from 2-D unicellular flow to 3-D flow is determined numerically for different sets of radii and longitudinal aspect ratios.

2. THE NUMERICAL APPROACH

2.1. *Formulation of the problem*

A porous annular layer bounded by two horizontal and concentric cylinders of axial length l is considered. The inner cylinder of radius r_i and the outer cylinder of radius r_0 are kept at uniform and constant temperatures T_i and T_c respectively, with $T_i > T_o$ (Fig. 1). The porous medium of porosity ε and permeability K, is saturated with an incompressible Newtonian fluid of kinematic viscosity ν.

This saturated porous medium is equivalent to an artificial fluid of heat capacity $(\rho c)^* = \varepsilon(\rho c)_f + (1-\varepsilon)(\rho c)_s$ and thermal conductivity λ^*. Two dimensionless parameters characterize the considered geometry: the radii ratio of the two cylinders, $R = r_o/r_i$, and the longitudinal aspect ratio, $A = l/r_i$ or $H = l/(r_o - r_i)$.

In addition to the Boussinesq approximation, several classical assumptions are made to simplify the formulation:

(i) Darcy's law is assumed to be valid;

(ii) the inertia terms and viscous dissipations are neglected;

(iii) the fluid is assumed to be in thermal equilibrium with the porous matrix.

The range of validity of the above cited assumptions are analysed in detail in Aniri and Vafai [18]. From their work it can be seen that the above assumptions can be invoked for a large range of practical applications.

Thus, the dimensionless form of the conservation of mass, momentum and energy are given as:

$$\nabla \cdot V = 0 \tag{1}$$

$$\nabla P + Ra^* kT + V = 0 \tag{2}$$

$$\frac{\partial T}{\partial t} + V \cdot \nabla T = \nabla^2 T \tag{3}$$

where V, P, and T refer to the velocity, the pressure and the temperature and $k = \boldsymbol{g}/\|\boldsymbol{g}\|$. The Rayleigh number of filtration, Ra^*, is defined as:

$$Ra^* = \frac{g\beta(T_i - T_0)(\rho c)_f K r_i}{\lambda^* \nu},$$

where $\boldsymbol{g}$ is the gravitational acceleration, β the coefficient of thermal expansion of the fluid, ρ its density and $(\rho c)_f$ its heat capacity.

In the present investigation, the 2-D and 3-D flows are assumed to be symmetrical with respect to the vertical plane including the cylinders' axis. This assumption is partially supported by the experimental results for 2D natural convection [1, 8, 10].

Based on the above assumptions, the following boundary conditions are imposed:

$$V_r = 0; \quad T = 1, \quad \text{at } r = 1$$

$$V_r = 0; \quad T = 0, \quad \text{at } r = R$$

$$V_\phi = \frac{\partial T}{\partial \phi} = 0, \quad \text{at } \phi = 0,\pi$$

$$V_z = \frac{\partial T}{\partial Z} = 0, \quad at\ Z = 0, A. \tag{4}$$

A conformal transformation is then used to shift from polar (r, ϕ, Z) to cartesian coordinates $(X = \ln r, Y = \phi, Z)$. The initial domain $[1, R] \times [0, \pi] \times [0, A]$ is then transformed in a cartesian domain: $[0, \ln R] \times [0, \pi] \times [0, A]$.

Taking the divergence of Darcy's law (equation 2), the velocity term is eliminated and the following transformed pressure and temperature equations are:

$$\frac{\partial^2 P}{\partial X^2} + \frac{\partial^2 P}{\partial Y^2} + \exp(2X)\frac{\partial^2 P}{\partial Z^2} = Ra^* \exp(X)\left(\cos Y \frac{\partial T}{\partial X} - \sin Y \frac{\partial T}{\partial Y}\right) \tag{5}$$

$$\frac{\partial^2 T}{\partial X^2} + \frac{\partial^2 T}{\partial Y^2} + \exp(2X)\frac{\partial^2 T}{\partial Z^2} = Ra^* \exp(X) T\left(\cos Y \frac{\partial T}{\partial X} - \sin Y \frac{\partial T}{\partial Y}\right) - \left(\frac{\partial P}{\partial X}\frac{\partial T}{\partial X} + \frac{\partial P}{\partial Y}\frac{\partial T}{\partial Y} + \exp(2X)\frac{\partial P}{\partial Z}\frac{\partial T}{\partial Z}\right) \tag{6}$$

with the boundary conditions:

$$X = 0: \quad T = 1, \quad \left.\frac{\partial P}{\partial X}\right|_{X=0} = Ra^* \cos Y \tag{7}$$

$$X = \ln R = \frac{1}{\alpha}: \quad T = 0, \quad \left.\frac{\partial P}{\partial X}\right|_{X=\ln R} = 0 \tag{8}$$

$$Y = 0, \pi: \quad \frac{\partial P}{\partial Y} = 0, \quad \frac{\partial T}{\partial Y} = 0; \tag{9}$$

$$Z = 0, A: \quad \frac{\partial P}{\partial Z} = 0, \quad \frac{\partial T}{\partial Z} = 0.$$

The set of equations (5)–(6) and boundary conditions (7)–(9) are also valid for the 2-D steady state if all the derivatives $\partial/\partial Z$ and $\partial^2/\partial Z^2$ are equal to zero.

The conformal mapping into a cartesian domain allows an easier use of the spectral method for obtaining the numerical solution of the problem. However, it should be noted that for the 3-D case, the presence of the term $\exp(2X)$ in the laplacian operator (equations (5)–(6)) may induce some numerical instabilities and reduce the efficiency of this transformation.

2.2. *Numerical procedure: a mixed Fourier–Chebyshev approximation*

In this section, the mixed Fourier–Chebyshev approximation is only presented for the 3-D case. For the 2-D case, a similar development using a stream function and temperature formulation has been used by a Charrier-Mojtabi *et al.* [8].

To solve equations (5)–(6) with the boundary conditions (7)–(9), the pressure P and the temperature T are expanded in terms of Fourier series in both azimuthal and axial periodic directions and as Chebyshev polynomials in the confined radial direction.

P and T are then expanded as follows, for the order N, L:

$$P_{N,L} = \sum_{n=0}^{N}\sum_{l=0}^{L} f_{nl}(X)\cos(nY)\cos(l\pi BZ) \tag{10}$$

$$T_{N,L} = 1 - \alpha X + \sum_{n=0}^{N}\sum_{l=0}^{L} g_{nl}(X)\cos(nY)\cos(l\pi BZ) \tag{11}$$

where $B = 1/A$.

Expansions (10) and (11) are inserted in equations (5) and (6), which are then properly projected on the Fourier basis function. If $Res_{N,L}$ denotes the residue of order N, L, the projections are:

$$\langle Res_{N,L}(P), \cos(pY)\cos(k\pi BZ)\rangle = 0 \qquad 0 \leqslant p \leqslant N; \quad 0 \leqslant k \leqslant L$$

$$\langle Res_{N,L}(T), \cos(pY)\cos(k\pi BZ)\rangle = 0 \quad 0 \leqslant p \leqslant N; \quad 0 \leqslant k \leqslant L.$$

The functions f_{pk} and g_{pk} are thus solutions of the second-order differential system:

$$f''_{pk}(x) - \left(\frac{p^2}{4\alpha^2} + \frac{L^2\pi^2B^2R^2}{4\alpha^2}\right) f_{pk}(x) = \frac{\pi^2B^2}{4\alpha^2}\left(k^2 \exp\left(\frac{x+1}{\alpha}\right) - L^2R^2\right) f_{pk} + C_{pk} \tag{12}$$

$$g''_{pk}(x) - \left(\frac{p^2}{4\alpha^2} + \frac{L^2\pi^2B^2R^2}{4\alpha^2}\right) g_{pk}(x) = \frac{\pi^2B^2}{4\alpha^2}\left(k^2 \exp\left(\frac{x+1}{\alpha}\right) - L^2R^2\right) g_{pk} + E_{pk} \tag{13}$$

where $x = 2\alpha X - 1$; $x \in [-1, +1]$

The expressions of the terms C_{pk} and E_{pk} are given in the Appendix. One can notice (equations (12)–(13)) that the treatment of the terms $f_{pk}\exp(x + 1/\alpha)$ and $g_{pk}\exp(x + 1/\alpha)$ is explicit.

The boundary conditions for the functions $f_{pk}(x)$ and $g_{pk}(x)$ are:

$$g_{pk}(-1) = g_{pk}(+1) = 0; \quad 0 \leqslant p \leqslant N, \quad 0 \leqslant k \leqslant L$$

$$f'_{pk}(+1) = 0; \quad 0 \leqslant p \leqslant N, \quad 0 \leqslant k \leqslant L$$

$$f'_{pk}(-1) = 0 \quad \text{except} \quad f'_{10}(-1) = Ra^*/2\alpha. \tag{14}$$

(14)

Equations (12) and (13) are discretized using the collocation-Chebyshev method (Canuto *et al.* [19]) with the Gauss-Lobatto points: $\{x_i = \cos(i\pi/(M-1)),\ i = 0 \ldots M-1\}$. Near the boundaries

$x = -1$ (i.e. $r = 1$) and $x = +1$ (i.e. $r = R$): this denser grid system ensures an accurate description of the radial boundary layers.

The functions $f_{pk}(x)$ and $g_{pk}(x)$ are expanded into truncated series of Chebyshev polynomials:

$$f_{pk}(x) = \sum_{m=1}^{M} \xi_{mpk} T_{m-1}(x)$$

and

$$g_{pk}(x) = \sum_{m=1}^{M} \theta_{mpk} T_{m-1}(x)$$

where $T_k(x) = \cos(k \arccos x)$.

With the collocation-Chebyshev method, all the computations are made in the physical space. Thus the unknowns are not the spectral coefficients ξ_{mpk} and θ_{mpk}, but the values of the functions $f_{pk}(x)$ and $g_{pk}(x)$ at the collocation points $\{x_i = \cos(i\pi/(M-1)), i = 0 \ldots M-1\}$:

$$[f_{pk}] = [f_{pk}(x_1), f_{pk}(x_2), \ldots f_{pk}(x_{M-2})]$$

and

$$[g_{pk}] = [g_{pk}(x_1), g_{pk}(x_2), \ldots g_{pk}(x_{M-2})]$$

The values of the functions $f_{pk}(x)$ and $g_{pk}(x)$ at the collocation points x_0 and x_{M-1} are deduced from the boundary conditions.

The linearized version of equations (12) and (13) are solved using a diagonalization procedure of the Chebyshev second-order derivative operation, D^{*2}_{CL}, properly modified to take into account the boundary conditions for the pressure (Neumann conditions) and the homogeneous boundary conditions for the temperature (Dirichlet conditions) (Haldenwang *et al.* [20]). The diagonalization itself is performed once, for all in a preprocessing step storage.

A special procedure is used to calculate $f_{00}(x)$ which appears in the development of the pressure P. First, it can be shown that (from equation (12))

$$f''_{00}(x) = \frac{Ra^* \exp((x+1)/2\alpha)}{8\alpha^2}(2\alpha g'_{10} + g_{10}).$$

Next, integrating the above equations results:

$$f'_{00}(x) = \frac{Ra^* \exp((x+1)/2\alpha)}{4\alpha} g_{10}.$$

The spectral coefficients of $f_{00}(x)$ are then evaluated from a recurrent equation using the spectral coefficients of $f'_{00}(x)$.

To ensure the stability of the numerical scheme a transient form of equation (13) is used:

$$\frac{\partial[g_{pk}]}{\partial t} = [D^{*2}_{CL} - \Lambda^2 I][g_{pk}] - [G_{pk}] \qquad (13')$$

where:

$$[g_{pk}] = [g_{pk}(x_1), g_{pk}(x_2), \ldots g_{pk}(x_{M-2})],$$

I is the unity matrix,

$$\Lambda^2 = \frac{p^2}{4\alpha^2} + \frac{L^2\pi^2 B^2 R^2}{4\alpha^2}$$

and

$$G_{pk} = \frac{\pi^2 B^2}{4\alpha^2}(k^2 \exp\left(\frac{x+1}{\alpha}\right) - L^2 R^2) g_{pk} + E_{pk}$$

This false transient procedure is not used to analyse unsteady phenomena, but it allows us to introduce in the computations different sets of initial conditions. These initial conditions can induce different steady solutions for the same set of values of the dimensionless parameters governing the problem.

The time integration is performed with an exponential fitting scheme of first-order [8], in the eigenvectors space of the Chebyshev second-order derivative operator, D^{*2}_{CL}, which takes into account the boundary conditions for the temperature. If $\tilde{g}_i^{n+1}$ indicates the value of $\tilde{g}_{pk}(x_i)$ at the time $(n+1)\Delta t$ in the eigenvectors space of D^{*2}_{CL}, and λ_i the eigenvalues of this operator, the exponential fitting scheme reads:

$$\tilde{g}_i^{n+1} = \tilde{g}_i^n - (1 - \exp[(\lambda_i - \Lambda^2)\Delta t]) \left[\tilde{g}_i^n - \frac{\tilde{G}_i^n}{\lambda_i - \Lambda^2}\right]. \qquad (15)$$

With the same notations, the diagonalization procedure for the pressure leads to:

$$\tilde{f}_i^{n+1} = \frac{\tilde{F}_i^n}{\lambda_{ip} - \Lambda^2}$$

where λ_{ip} are the eigenvalues of the Chebyshev second-order derivative operator modified to take into account the boundary conditions for the pressure.

The convergence criterion is based on both the global Nusselt number Nu_g^*, which characterizes the heat transfer rate between the two cylinders, and the local Nusselt number $Nu^*(Z)$ calculated in constant Z planes:

$$Nu_g^* = 1 - 2'_{g_{00}}(x = -1)$$

and (16)

$$Nu^*(Z) = 1 - 2\sum_{l=0}^{L} g'_{0l}(x = -1)\cos(l\pi BZ).$$

The convergence of the spectral coefficients, ζ_{mpk} and θ_{mpk}, is also considered. The convergence test applied to each of 50 iterations is:

$$\frac{\mathrm{Max}_{mpk} |\zeta_{mpk}^{n+1} - \zeta_{mpk}^n|}{\mathrm{Max}_{mpk} |\zeta_{mpk}^{n+1}|} < \delta$$

with $\delta = 5\,10^{-4}$ for the 3-D case and $\delta = 10^{-4}$ or 10^{-5} for the 2-D case (depending on the value of R and Ra^*).

3. MULTICELLULAR 2-D FLOWS ANALYSIS

3.1. *Comparison with the results obtained using a* Ψ–T *formulation*

The results obtained with this new P–T formulation have been first compared to those obtained using the stream function and temperature (Ψ–T) formulation [8]. In both cases, different flow structures and isotherms may appear for the same values of Ra^* and R depending on the initial conditions introduced in the computations. These initial conditions have been obtained by means of an identification between the development of the temperature using the full Fourier–Galerkin method [8] and the Fourier–Chebyshev method. Thus the functions $g_n(x)$ are developed as follows: $g_n(x) = \Sigma_{m=1}^{M} b_{mn} \sin(m\pi(x+1)/2))$ and are computed at the collocation points x_i.

In our previous work [8], it has been shown that the introduction of initial coefficients in the computations $b_{ij}^0 = 0.001\ \forall i,j$ induced an unicellular flow. With all $b_{ij}^0 = 0$, except $b_{13}^0 = -0.1$, $b_{14}^0 = +0.1$, $b_{15}^0 = -0.1$, a bicellular flow is obtained and with the set: all $b_{i,j}^0 = 0$, except $b_{16}^0 = -0.2$, $b_{17}^0 = +0.2$, $b_{18}^0 = -0.2$, $b_{19}^0 = +0.2$ a tricellular flow is induced.

For all the cases which were investigated in this work, ($Ra^* \in [10, 350]$, $R = 2^{1/4}$, $2^{1/2}$, 2) a very good agreement has been found between the results obtained using the two formulations. With the P–T formulation, the stream function is calculated at the end of the computations. The stream function Ψ is represented by:

$$\Psi(X, Y) = \sum_{n=1}^{N} h_n(X) \sin(nY) \tag{17}$$

where

$$ph_p(X) = Ra^* \exp(X)(1-\alpha X)\,\delta_{1,p} + Ra^* \frac{\exp(X)}{2}(g_{p-1} + g_{p+1} + g_{1-p}) - f'_p(X).$$

Figure 2(a), (b) and (c) shows the isotherms on the right and the pressure fields on the left, for the case $Ra^* = 200$ and $R = 2$. For this configuration, with the approximation $M \times N = 30 \times 30$, a 2-D unicellular (Fig. 2(a)), bicellular (Fig. 2(b)) or tricellular flow (Fig. 2(c)) can be obtained. The flow configuration consist of one, two or three cells on half the domain, respectively. These figures can be compared to Fig. 2(d), (e) and (f), obtained with the Ψ–T formulation for the same Ra^* and R combination and the same set of initial solutions.

It can be seen that the pressure field is very weakly affected by the flow structure modifications. This result was observed for all the cases studied in this work, as the pressure field remained quite stratified despite the free convective field. The same behaviour is observed for natural convection in a horizontal annulus filled with a fluid (Cheddadi *et al.* [15]).

3.2. *Bifurcation phenomena for* $R = 2$ *and* $R = 2^{1/2}$: *influence of the truncation*

The numerical determination of the bifurcation points between the 2-D unicellular flow and multicellular flows requires an accurate description of the basic flows. In previous work [8], Charrier-Mojtabi *et al.* have shown that 30 collocation points are sufficient to describe all the flow configurations, while 80 Fourier-modes in the ϕ-direction are barely sufficient for the description of multicellular flows. Previous investigators [5, 6] have determined these 2-D multicellular flows using only low orders of approximation, not exceeding 20×20 with the full Fourier–Galerkin method. So, in this section, higher orders of approximation, up to $M = 45$ collocation points in the radial direction and $N = 135$ Fourier modes in the azimuthal direction have been considered.

The calculations were first performed to characterize the transition between the 2-D unicellular flow and the 2-D bicellular flow observed experimentally by Charrier-Mojtabi *et al.* [8] for $R = 2$ and for a large range of Ra^*. The average Nusselt numbers for those two flows are reported in Table 1 and the corresponding curves $Nu^*g = F(Ra^*)$ are plotted in Fig. 3.

The process of determination of the bifurcation points is shown in Fig. 3. From a converged 2-D bicellular solution obtained using initial conditions specified in Section 3.1, the Rayleigh number is decreased step by step and the converged steady-state solution is used as initial condition for the next step. This process is continued until the 2-D bicellular flow transits to a 2-D unicellular one. The lower branch of Fig. 3 is obtained by increasing the Rayleigh number, the first calculation using initial conditions inducing a 2-D unicellular flow. One can notice that the difference between the global Nusselt number of the two modes decreases continuously to zero when the Rayleigh number is closed to the critical value and that no hysteresis loop has been obtained as mentioned by Barbosa *et al.* [21]. Thus, the critical value of the Rayleigh number corresponding to this transition, for $R = 2$, is:

$$60.5 < Ra_c^* < 61.5.$$

This value, determined with the order of approximation of 30×95, is lower than the value obtained numerically by Rao *et al.* using the Galerkin method at low approximation [5] ($Ra_c^* = 65.5 \pm 0.5$) and close to the one obtained, with a linear stability analysis, by Himasekhar and Bau [6] ($Ra_c^* \approx 62$).

For the case $R = 2^{1/2}$, the results are reported in Table 2. The critical Rayleigh number obtained for this transition, using an order of approximation of 30×95, is:

$$111.5 < \mathrm{Ra}_c^* < 112.$$

Himasekhar and Bau [6] using a linear stability analysis, found $Ra_c^* \approx 112$. However, using another method

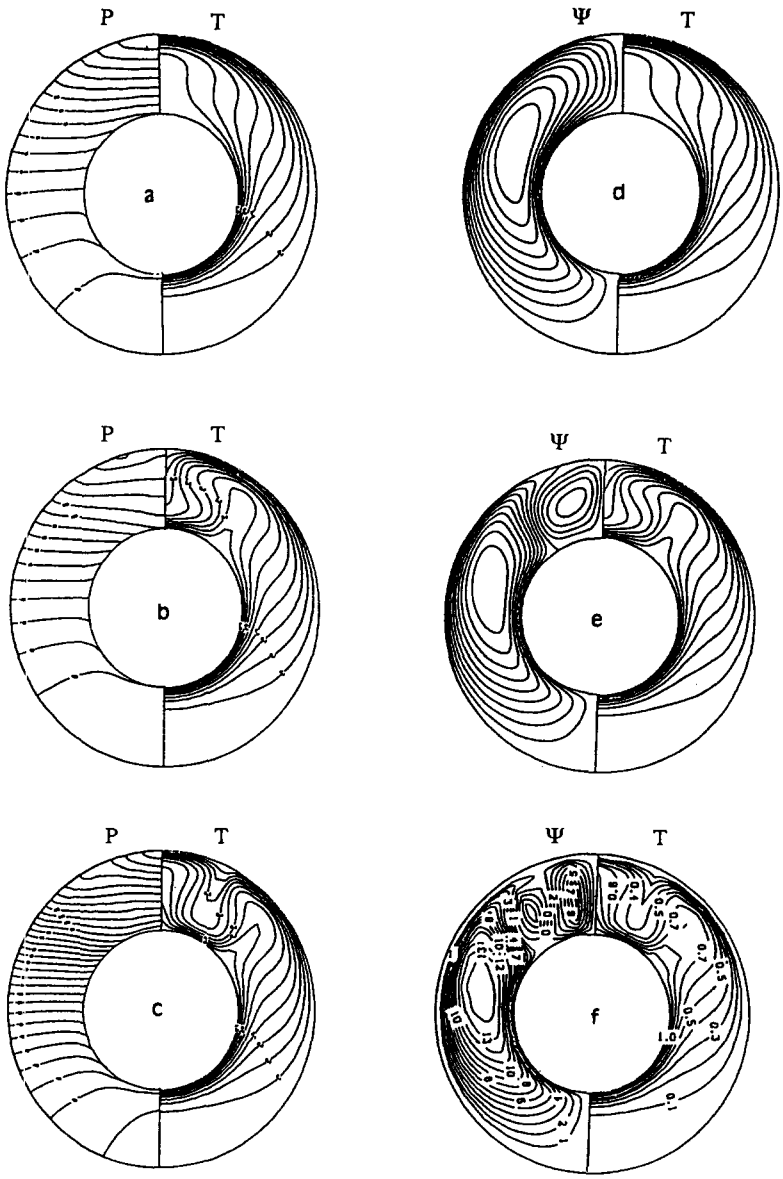

Fig. 2. $Ra^* = 200$, $R = 2$. Pressure field and isotherms: (a) 2-D unicellular flow; (b) 2-D bicellular flow; (c) 2-D tricellular flow. Streamlines and isotherms: (d) 2-D unicellular flow; (e) 2-D bicellular flow; (f) 2-D tricellular flow.

Table 1. Transition from 2-D unicellular flow to 2-D bicellular flow, for $R = 2$; $M \times N = 30 \times 95$

Ra^*	Nu_g^* unicellular flow	Nu_g^* bicellular flow
55	1.397	—
60	1.451	—
61.5	1.468	1.482
62.5	1.479	1.508
65	1.506	1.562
70	1.560	1.657
80	1.666	1.807
100	1.867	2.053
120	2.053	2.269
150	2.309	2.544

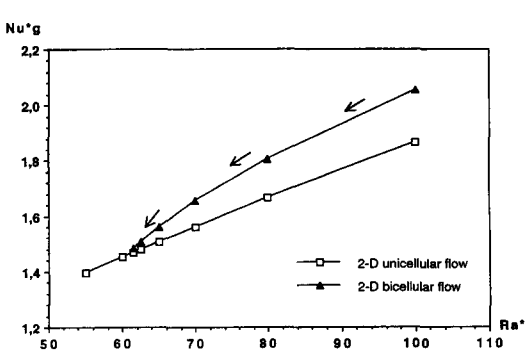

Fig. 3. Bifurcation point 2-D unicellular flow to 2-D bicellular flow for $R = 2$ ($M \times N = 30 \times 95$).

Table 2. Transition from 2-D unicellular flow to 2-D bicellular flow, for $R = 2^{1/2}$; $M \times N = 30 \times 95$

Ra^*	Nu_g^* unicellular flow	Nu_g^* bicellular flow
100	1.0791	
105	1.0866	
107	1.0886	
109	1.0916	
110	1.0933	
110.5	1.0943	
111	1.0948	
111.5	1.0956	
112	1.0964	1.1014
115	1.1013	1.1208
120	1.1096	1.1455

based on the analysis of the convergence of the regular perturbation expansion $Nu_g^* = f(Ra^{*2})$, these authors found a critical Rayleigh number of $Ra_c^* = 120 \pm 3$.

So, considering a higher order of approximation leads to a more accurate determination of both the solutions and the transition points.

Our numerical analysis shows the existence of two stable solutions for $Ra^* > Ra_c^*$, for $R = 2$ and $R = 2^{1/2}$. For these two values of R, Himasekhar and Bau [6] have shown that the loss of uniqueness occurs as a result of the appearance of an isolated solution branch and that the two branches of solution (2-D unicellular and bicellular) are linearly stable which is in good agreement with our numerical results. Then, they show that these two branches of solution lose their stability via a Hopf bifurcation for high Rayleigh numbers. On the contrary, for $R = 2^{1/4}$ and $2^{1/8}$, these authors have shown that the transition between the 2-D unicellular flow and 2-D multicellular flow occurs via a perfect bifurcation: one solution branch loses stability while another one gains it.

3.3. *On the existence of the 2-D tricellular flow for* R = 2

Then, the same process was utilized to investigate the transition between the 2-D unicellular and the 2-D tricellular flows. However this led to some difficulties. Figure 4(a) and (b) show the time variation of the average Nusselt number, for $Ra^* = 200$ and $R = 2$ for 2-D bicellular and tricellular flows respectively, using an approximation $M = 30$, $N = 95$. We find that the 2-D tricellular flow transits to an unicellular after 6000–7000 time steps, while the bicellular flow remains stable even after 12 000 time steps. Other computations made for $R = 2$ and higher values of the Rayleigh number, show that the 2-D tricellular flow does not subsist for the approximation $M \times N = 30 \times 95$. Using a higher order of approximation $M = 45$, $N = 135$, for the same configuration ($Ra^* = 200$ and $R = 2$), the 2-D tricellular flow disappears between 18 000 and 20 000 iterations and transits to the 2-D unicellular flow. The same result is

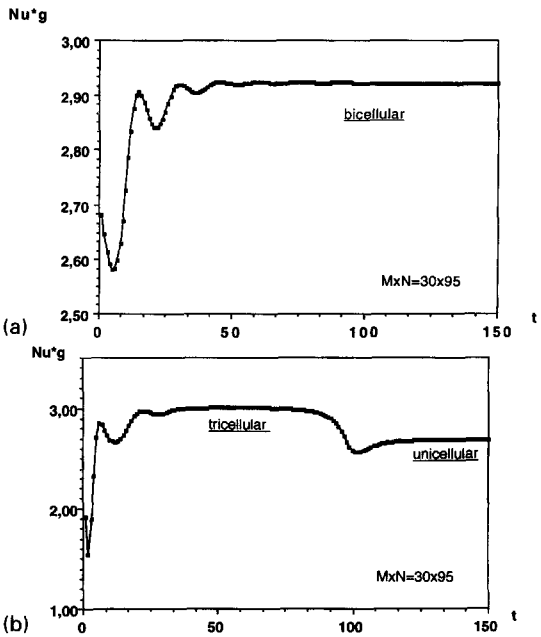

Fig. 4. $Nu_g^* = f(t)$ for $Ra^* = 200$, $R = 2$: (a) 2-D bicellular flow; (b) 2-D tricellular flow.

obtained for $Ra^* = 300$. For Rayleigh numbers higher than 350 oscillating flows occur.

So, for $R = 2$, a 2-D tricellular flow appears for lower order approximations, but this flow disappears for higher order approximations (see Table 3 for $Ra^* = 200$), while the 2-D bicellular flow subsists for higher order approximations. These numerical results appear to agree with experimental visualizations of the thermal field using the Christiansen effect and presented in previous work [8], for which 2-D bicellular structures have been observed while 2-D tricellular flows have never been observed (for the case $R = 2$). For this case, the tricellular flow is only a mathematical solution which is linearly unstable. In this work, the steady solutions are obtained through a time evolution. The numerical residue of the temporal discretization can be seen as an infinitesimal perturbation of the system. Thus, this method allows only to keep the linearly stable solutions, steady or not. Recent mathematical developments proposed by [22] using a Newton method, allow the calculation of linearly unstable solutions.

Table 3. Analysis of the tricellular flow for $R = 2$: influence of the order of approximation

Ra^*	M	N	Nu_g^*	Flow
200	16	16	2.98–3.02	Tricellular
200	20	20	2.683	Unicellular
200	30	30	3.001	Tricellular
200	40	40	2.995	Tricellular
200	20	80	3.000	Tricellular
200	30	95	2.681	Unicellular
200	45	135	2.679	Unicellular

Table 4. Influence of the orders of approximation $M \times N \times L$: $R = 2$, $H = 2$

Ra^*	M	N	L	Nu_g^* 3-D flow
60	16	12	12	1.471
60	16	16	16	1.479
75	16	12	12	1.707
75	16	16	16	1.716
100	8	8	8	1.879
100	16	12	12	1.953
100	16	16	16	1.960
120	8	8	8	1.984
120	16	12	12	2.169
120	16	16	16	2.120

4. ANALYSIS OF THE 3-D FLOWS

One of the interests of this new 2-D P–T formulation is due to the fact that it may be naturally extended to a 3-D one. However, as it has been indicated in Section 2.1, the presence of the term $\exp(2X)$ in the Laplacian operator (equations (5) and (6)), for the 3-D case, induces numerical instabilities. These instabilities are due to the time step necessary for the iterative process to converge to the steady solution [23]. The explicit treatment of the terms $f_{pk}(X)\exp(2X)$ and $g_{pk}(X)\exp(2X)$ penalizes this last. However, when low orders of approximation are considered, the time step remains acceptable in order that the system converges to the expected steady state. Therefore, the 3-D study has been limited to low orders of approximation up to $M \times N \times L = (16)^3$. The same two values of R have been considered, i.e. $R = 2$ and $R = 2^{1/2}$, while the longitudinal aspect ratio, H, was varied between 0.5 and 2. Calculations have been made with Rayleigh numbers close to the critical value of the transition between the 2-D unicellular flow and the 3-D flow. For these values of Ra^*, the flow is still predominantly two dimensional except at the upper part of the layer and approximation $M \times N \times L = (16)^3$ is sufficient to describe the 3-D effects. The influence of the order of approximation on the solution is reported in Table 4, for the case $R = 2$, $H = 2$: it can be seen that the change of the approximation from $16 \times 12 \times 12$ to $16 \times 16 \times 16$ induces less than 6‰ change in the mean Nusselt number for Ra^* varying from 60 to 100 and a change of 2.5% for $Ra^* = 120$.

4.1. *Structure of the 3-D spiral flows and temperature fields*

If the initial conditions correspond to 3-D perturbations oriented in axial direction (Z), then 3-D spiral flows are generated for values of Ra^* larger than a critical value, Ra_c^*. This critical value, which depends on R and H, has been determined numerically for two sets of values of R and H.

Figure 5 shows the isothermal lines in r-Z planes for $R = 2$ and $H = 2$ and for $Ra^* = 100$. The thermal field at the top of the annulus (Fig. 5(a)) is very similar to the one observed for a horizontal porous layer heated from below. As ϕ increases to $\phi = 90°$ (Fig. 5(b), (c), (d)), the temperature gradient in the axial direction decreases and ultimately is negligible for $\phi = 90°$. The symmetry of the thermal field with respect to the vertical plane $Z = H/2$ can be seen clearly in these figures.

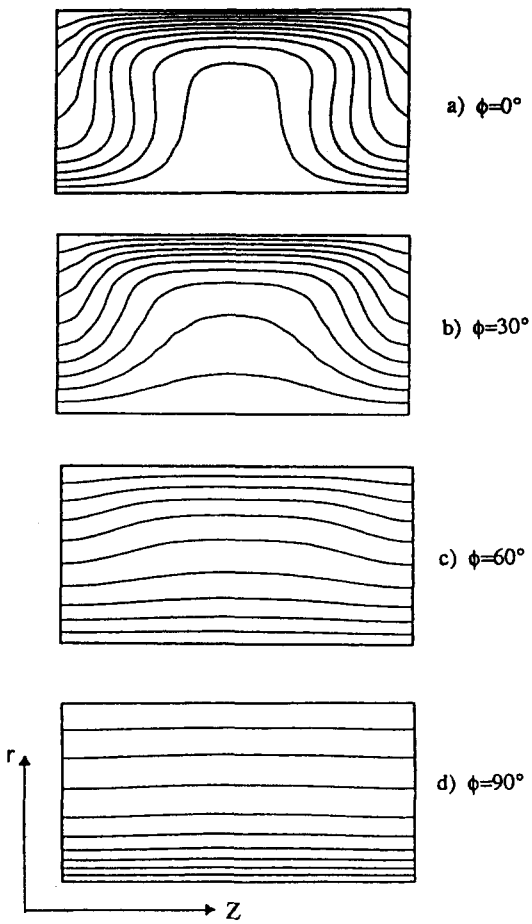

Fig. 5. Isothermal lines in planes (a)$\phi = 0°$; (b) $\phi = 30°$; (c) $\phi = 60°$; (d) $\phi = 90°$. $Ra^* = 100$, $R = 2$, $H = 2$.

Temperature contours for vertical planes $Z = 0$, $Z = H/4$ and $Z = H/2$ are shown in Fig. 6 (Fig. 6(a), (b) and (c), respectively). In the plane $Z = H/2$, the temperature field resembles the one obtained for the 2-D unicellular flow ($Ra^* = 100$, $R = 2$). Deformations appear at the top of the annulus for $Z = H/4$, and for $Z = 0$, the temperature distribution becomes quite similar to the corresponding 2-D bicellular flow.

A graphical software has been used to visualize the 3-D velocity field. On Fig. 7, the velocity field is reported for $Ra^* = 100$, $R = 2$, $H = 2$ in planes $\phi = 0°$ (Fig. 7(a)), $\phi = 10°$ (Fig. 7(b)), and $\phi = 20°$ (Fig. 7(c)). In accordance with the thermal field, the flow at the top of the annulus is similar to a couple of Benard cells in a horizontal porous layer. The spiral aspect of this 3-D flow clearly appears in planes $\phi = 10°$ and $\phi = 20°$. The cellular flow becomes weaker at lower planes for $\phi > 60°$. The flow remains then quite 2-D as indicated in Fig. 7(d) where the flow

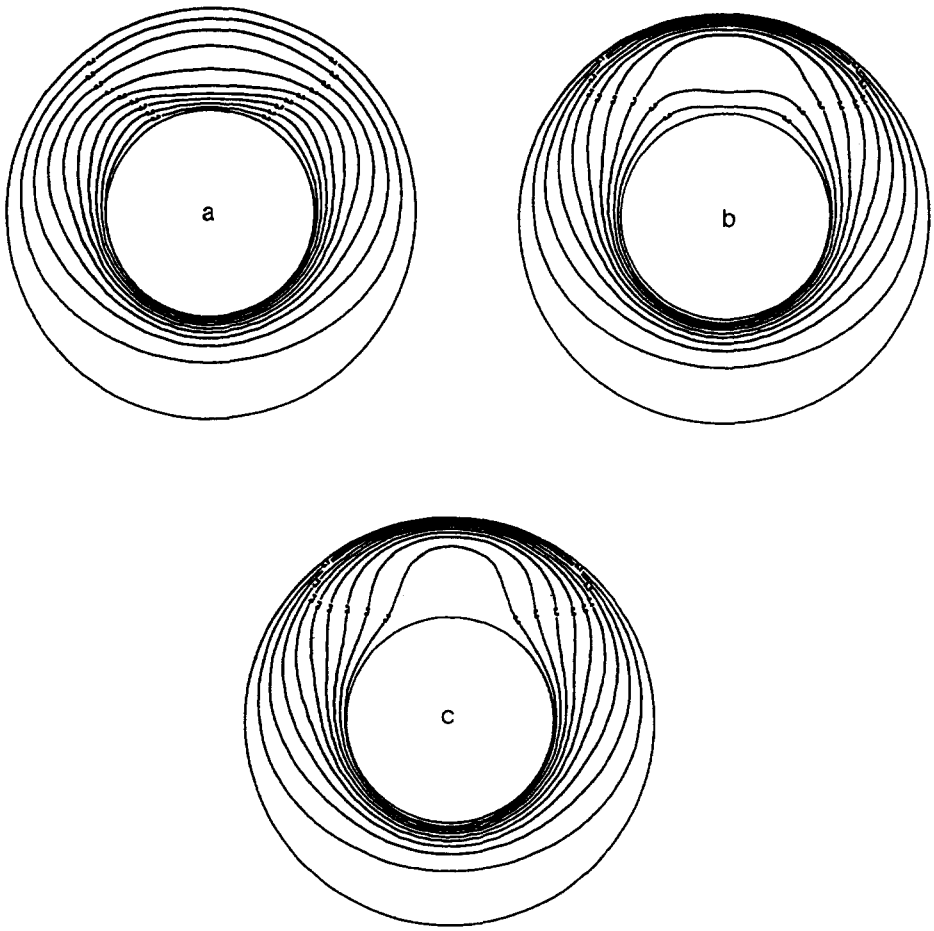

Fig. 6. Isothermal lines in planes: (a) $Z = 0$; (b) $Z = H/4$; (c) $Z = H/2$. $Ra^* = 100$, $R = 2$, $H = 2$.

field is plotted in a r-section near the outer cylinder and in two Z-sections, symmetrical with respect to the vertical midplane (Fig. 7(e)). These results are in good agreement with those obtained by Rao *et al.* [14].

The results obtained for the case $R = 2^{1/2}$ and $H = 2$, are quite close to those obtained for $R = 2$ and $H = 2$ and thus are not presented here. For the case $R = 2$ and $H = 1$, the isothermal lines show the presence of one cell at the top of the annulus extending in the axial direction (Fig. 8). This result confirms the influence of the longitudinal aspect ratio, H, on the development of three dimensional axial disturbances which governs the number of cells along the axial direction.

4.2. *Transition between 2-D and 3-D convection regime*

For a given set of values of R and H, a critical value of the Rayleigh number exists for which the 2-D unicellular flow and the 3-D flow have the same heat transfer rate. The determination of this point requires a special procedure. From a converged 3-D solution, Ra^* is decreased step by step. For each step, the converged steady state solution is calculated and used as initial condition for the next step. When the critical value Ra_c^* is reached, the 3-D flow converges slowly to a 2-D unicellular one. Near this point a great number of iterations is required to obtain the converged solution. For $R = 2$ and $H = 2$, the average Nusselt numbers for the two flows are reported in Table 5. As can be seen in this table, the transition between the 2-D unicellular flow and the 3-D flow corresponds to:

$$55 < Ra_c^* < 60.$$

Table 5. Transition from 2-D unicellular flow to 3-D flow, for $R = 2$; $H = 2$; $M \times N \times L = 16 \times 16 \times 16$

Ra^*	Nu_g^* 2-D unicellular flow	Nu_g^* 3-D flow
40	1.234	
45	1.289	
50	1.343	
55	1.397	
60	1.451	1.479
75	1.615	1.716
100	1.867	1.960
120	2.053	2.120

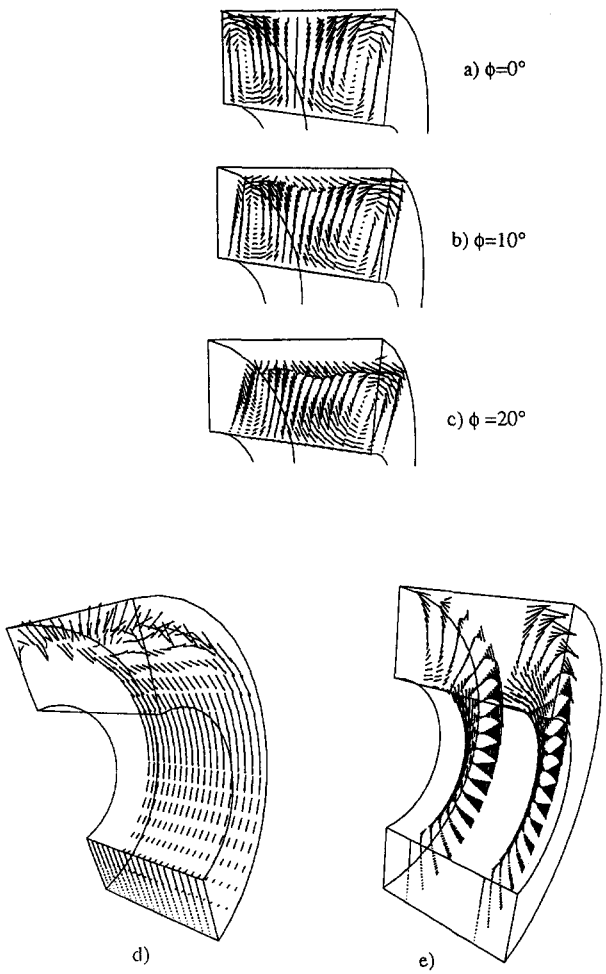

Fig. 7. 3-D velocity field for $Ra^* = 100$, $R = 2$, $H = 2$.

This result is in relatively good agreement with experimental results of Caltagirone [1] who obtained Ra_c^* exp. $= 65 \pm 4$ for $R = 2$ and $H = 20$. A stability analysis [1] shows that this critical Rayleigh number does not change if H is greater than a value close to $H = 1.5$: thus the above comparison can be done. This latter has been developed in previous works [24, 25].

For the case $R = 2^{1/2}$ and $H = 2$, the results are reported in Table 6. We find that Ra_c^* is between 90 and 100 which agrees with the results of the linear stability analysis of Caltagirone [1] leading to $Ra_c^* = 103.4$.

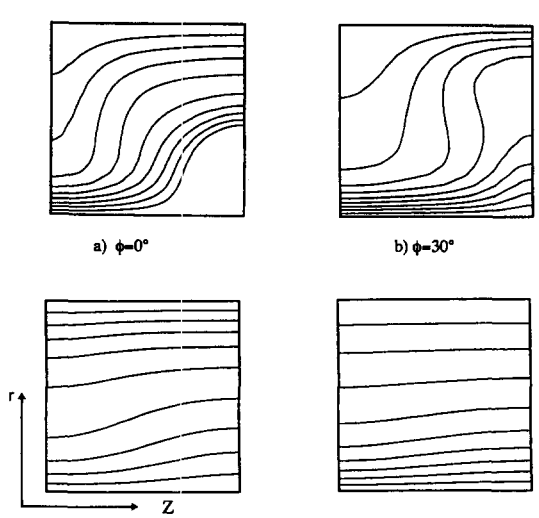

Fig. 8. Isothermal lines in planes: (a) $\phi = 0°$; (b) $\phi = 30°$; (c) $\phi = 60°$; (d) $\phi = 90°$. $Ra^* = 100$, $R = 2$, $H = 1$.

Table 6. Transition from 2-D unicellular flow to 3-D flow for $R = 2^{1/2}$; $H = 2$; $M \times N \times L = 16 \times 16 \times 16$

Ra^*	Nu_g^* 2-D unicellular flow	Nu_g^* 3-D flow
70	1.039	
80	1.051	
90	1.064	
100	1.079	1.108
120	1.109	1.194
150	1.165	1.250
200	1.266	1.326

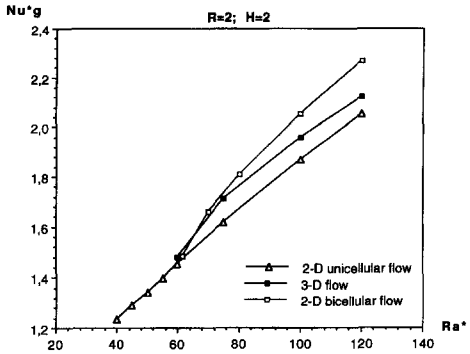

Fig. 9. Comparison between average Nusselt numbers for 2-D flows and 3-D flow $R = 2$; $H = 2$.

4.3. *Influence of the flow pattern on the heat transfer rate*

For $R = 2$ and $H = 2$, the heat transfer rate expressed by the average Nusselt number plotted as a function of the Rayleigh number is represented in Fig. 9, for the 2-D unicellular and bicellular flow, and for the 3-D flow. As it might be expected, the 3-D spiral flow produces a higher heat transfer rate than the 2-D unicellular one. However, the difference obtained is rather small. It can also be seen that the heat transfer rate for the 3-D flow is smaller than the 2-D bicellular one. These results agree with the numerical results reported by Rao *et al.* [14]. For the 3-D case a good agreement is found with the experimental results of Caltagirone [1] obtained for $R = 2$ and $H = 20$, due to the periodicity of the flow along the axial direction.

To complete this study, more computations have to be done to allow us to predict the flow (2-D multicellular flow or 3-D flow) that will set in after the 2-D unicellular one when the Rayleigh increases for a given value of the couple (R, H). The stability analysis performed in refs. [1] and [6] don't allow us to forecast which flow will take place. For the case of narrow gaps ($R \ll 2^{1/2}$), Charrier-Mojtabi *et al.* [26] using an analytical analysis, has determined a criterion for which a 2-D multicellular structure can appear before a 3-D one.

5. CONCLUSION

A numerical investigation of natural convection in a saturated porous horizontal annulus using a pressure and temperature formulation and a mixed Fourier–Galerkin-collocation-Chebyshev method is presented. Experimental studies to determine the onset of the different flows (2-D unicellular or multicellular, 3-D) are not easy to carry out. So, numerical experimentation and/or stability analysis are used to investigate all these problems where multiple solutions appear. In this study, the 2-D multicellular flows have been analysed using high orders of approximation. Thus an accurate evaluation of the critical Rayleigh number for the transition between the 2-D unicellular flow and these flows, has been done for $R = 2$ and $R = 2^{1/2}$. For the case $R = 2$, the computations show that the 2-D tricellular flow is unstable and changes, after a long period of time, towards the 2-D unicellular one. The mixed Fourier–Chebyshev method is conceptually more adapted than the full Fourier–Galerkin method, used in the previous works, to analyse the multiple mathematical solutions of the problem.

For the 3-D flows, the study has been limited to low orders of approximation, due to the resulting instabilities involved by the presence of the $\exp(2X)$ term in the governing equations. Therefore, only 3-D flows close to the transition region, 2-D unicellular flow-3-D flow, have been considered. For these flows, the approximation used in the present work, $M \times N \times L = (16)^3$, is sufficient to describe the 3-D effects. The numerical results show the complex 3-D spiral flow patterns where 3-D effects are localized at the top of the annulus. For $R = 2$, $H = 2$ and $R = 2^{1/2}$, $H = 2$, the bifurcation point between the 2-D unicellular flow and the 3-D flow has been determined numerically. A good agreement was observed with both experimental results and stability analysis results of Caltagirone [1] for the case $R = 2$. However, higher orders of approximation must be considered to describe these 3-D flows for higher Rayleigh numbers. For the 3-D case, the hypothesis of symmetry with respect to the vertical plane including the axis of the two cylinders seems to be too restrictive. The author also believes that stability analysis are still necessary to understand the complete physical mechanisms of the transition from the 2-D unicellular flow towards either a 2-D multicellular or a 3-D flow.

Acknowledgements—The author would like to acknowledge the C.N.U.S.C. (National Center of Computations of Montpellier) for its financial support. He is also grateful to Prof. Vafai K. for useful discussions.

REFERENCES

1. Caltagirone, J. P., Thermoconvective instabilities in a porous medium bounded by two concentric horizontal cylinders. *Journal of Fluid Mechanics*, 1976, **76,** 337–362.
2. Burns, P. J. and Tien, C. L., Natural convection in porous medium bounded by concentric spheres and horizontal cylinders. *International Journal of Heat and Mass Transfer*, 1979, **22,** 929–939.
3. Mojtabi, A., Ouazar, D. and Charrier-Mojtabi, M. C., An efficient finite element code for 2-D steady state in a porous annulus. *Proceedings of the International Conference on Numerical Methods for Thermal Problems*, Vol. 5, Part 1, Montreal, Canada, 1987, pp. 644–654.
4. Charrier-Mojtabi, M. C. and Caltagirone, J. P., Numerical simulation of natural convection in an annular porous layer by spectral method. *Proceedings of the International Conference of Numerical Methods for Non-Linear Problems*, Swansea, U.K. 1980, pp. 821–828.
5. Rao, Y. F., Fukuda, K. and Hasegawa, S., Steady and transient analysis of natural convection in a horizontal porous annulus with Galerkin method. *Journal of Heat Transfer*, 1987, **109,** 919–927.
6. Himasekhar, K. and Bau, H. H., Two-dimensional bifurcation phenomena in thermal convection in horizontal concentric annuli containing saturated porous media. *Journal of Fluid Mechanics*, 1988, **187,** 267–300.
7. Mojtabi, A. and Charrier-Mojtabi, M. C., Analytical

solution of steady natural convection in an annular porous medium evaluated with a symbolic algebra code. *Journal of Heat Transfer*, 1992, **114,** 1065–1067.
8. Charrier-Mojtabi, M. C. and Mojtabi, A., Azaiez, M. and Labrosse, G.. Numerical and experimental study of multicellular free convection flows in an annular porous layer. *International Journal of Heat and Mass Transfer*, 1991, **34,** 3061–3074.
9. Himasekhar, K. and Bau, H. H., Large Rayleigh number convection in a horizontal eccentric annulus containing saturated porous media. *International Journal of Heat and Mass Transfer*, 1986, **29,** 703–712.
10. Cloupeau, M. and Klarsfeld, S., Visualization of thermal fields in saturated porous media by Christiansen effect. *Applied Optics*, 1973, **12,** 198–204.
11. Bau, H. H., McBlane, G. and Sarferstein, I., Numerical simulation of thermal convection in an eccentric annulus containing porous media. ASME 83 WA/HT 34, 1983.
12. Fukuda, K., Takuta, Y., Hasegawa, S., Shimomura, S. and Sanokawa K., *Three-Dimensional Natural Convection in a Porous Medium Between Concentric Inclined Cylinders*. A.S.M.E., Vol. HTD-8, Orlando, U.S.A., 1980, pp. 97–103.
13. Charrier-Mojtabi, M. C., Mojtabi, A. and Caltagirone, J. P., Three dimensional convection in a horizontal porous layer. *Euromech* 138, Karlsruhe, 1981, pp. 75–77.
14. Rao, Y. F., Fukuda, K. and Hasegawa, S., A numerical study of three dimensional natural convection in a horizontal porous annulus with Galerkin method. *International Journal of Heat and Mass Transfer*, 1988, **31,** 695–707.
15. Cheddadi, A., Caltagirone, J. P., Mojtabi, A. and Vafai, K., Free two-dimensional convective bifurcation in a horizontal annulus. *Journal of Heat Transfer*, 1992, **114,** 99–106.
16. Rao, Y. F., Miki, Y., Fukuda, K., Takata, Y. and Hasegawa, S., Flow patterns of natural convection in horizontal cylindrical annuli. *International Journal of Heat and Mass Transfer*, 1985, **28,** 705–714.
17. Vafai, K. and Ettefagh, J., An investigation of transient three-dimensional buoyancy-driven flow and heat transfer in a closed horizontal annulus. *International Journal of Heat and Mass Transfer*, 1991, **34,** 2555–2570.
18. Aniri, A. and Vafai, K., Analysis of dispersion effects and non thermal equilibrium, non-Darcian, variable porosity incompressible flow through porous medium. *International Journal of Heat and Mass Transfer*, 1994, **37,** 939–954.
19. Canuto, C., Hussaini, M. Y., Zang, T. A. and Quarteroni, A., *Spectral Methods in Fluids Dynamics*. Springer, Berlin, 1988.
20. Haldenwang, P., Labrosse, G., Abboudi, S. and Deville, M., Chebyshev 3-D spectral and 2-D pseudospectral solvers for the Helmholtz equation. *Journal of Computational Physics*, 1984, **55,** 277–290.
21. Barbosa, J. P. and Saatdjian, E., Natural convection in porous horizontal cylindrical annulus. *Journal of Heat Transfer*, 1994, **116,** 621–626.
22. Dijkstra, H. A., On the structure of cellular solutions in Rayleigh–Benard–Marangoni flows in small aspect ratio containers. *Journal of Fluid Mechanics*, 1992, **243,** 73–102.
23. Fletcher, C. A. J., *Computational Techniques for Fluids Dynamics*, Vol. 1. Springer, Berlin, 1988.
24. Charrier-Mojtabi, M. C. and Mojtabi, A., Numerical simulation of three-dimensional free convection in a horizontal porous annulus. *Proceedings of the International Heat Transfer Conference*, Vol. 2. Brighton, U.K., 1994, 319–324.
25. Charrier-Mojtabi, M. C., Etude numérique, théorique et expérimentale des écoulements thermoconvectifs bidimensionnels et tridimensionnels en couche annulaire poreuse horizontale. Thèse de Doctorat d'Etat, University of Bordeaux I, France, 1993.
26. Charrier-Mojtabi, M. C. and Mojtabi, A., Stabilité des écoulements de convection naturelle en espace annulaire poreux horizontal. *C.R. Academie de Science* Paris, t. 320, série IIb, pp. 177–183, 1995.

APPENDIX

The expressions of the terms $C_{pk}(x)$ and $E_{pk}(x)$ of equations (12) and (13) are issued from the corresponding terms expressed with the variable X and denoted respectively $C^1_{pk}(X)$ and $E^1_{pk}(X)$:

$$C^1_{pk}(X) = Ra^* e^X \delta_1 [-2\alpha \delta_{1p} \delta_{k0} \delta_2 + \tfrac{1}{2}(g'_{1+p,k} + g'_{1-p,k} + g'_{1-p,k} + (1-p)g_{1-p,k} + (1+p)g_{1+p,k} - (p-1)g_{p-1,k})]$$

$$\begin{aligned} E^1_{pk}(X) = {} & (1-\alpha X) Df_{pk} + \alpha f'_{pk} \\ & + \frac{\delta_1 \delta_2}{4} \sum_{n=0}^{N} \sum_{r=0}^{N} \left[\left(\frac{Df_{n,k-r}}{\delta_2} + Df_{n,r-k} + Df_{n,k+r} \right) \right. \\ & * \left(\frac{g_{p-n,r}}{\delta_1} + g_{p+n,r} + g_{n+p,r} \right) \\ & - \left(\frac{f'_{n,k-r}}{\delta_2} + f'_{n,r-k} + f'_{n,k+r} \right) \\ & * \left(\frac{g'_{p-n,r}}{\delta_1} + g'_{p+n,r} + g'_{n-p,r} \right) \\ & - n \left(\frac{f_{n,k-r}}{\delta_2} + f_{n,r-k} + f_{n,k+r} \right) \\ & * ((n+p)g_{p+n,r} + (n-p)g_{n-p,r} - (p-n)g_{p-n,r}) \\ & - e^{2X}(B_{r-k} f_{n,r-k} + B_{k+r} f_{n,k+r} - B_{k-r} f_{n,k-r}) \\ & \left. * \left(\frac{g_{p-n,r}}{\delta_1} + g_{p+n,r} + g_{n-p,r} \right) B_r \right] \end{aligned}$$

with

$\delta_1 = \frac{1}{2}$ for $p = 0$ and $\delta_1 = 1$ for $p > 0, \delta_2 = \frac{1}{2}$ for $k = 0$

and $\delta_2 = 1$ for $k > 0$ $B_r = r\pi B$ $\forall r \in N$

the symbol D is defined as follows:
$Df_{mn} = f''_{mn} - (m^2 + B_n^2 e^{2X}) f_{mn}$.